Electronic supplementary information

Bio-inspired progressive motile sperm separation using joint rheotaxis and boundary-following behavior

Mohammadjavad Bouloorchi Tabalvandani[†], Saeed Javadizadeh[†], and Majid Badieirostami*

MEMS Lab, School of Electrical and Computer Engineering, College of Engineering, University of Tehran, Tehran, Iran.

*Corresponding author: mbadiei@ut.ac.ir

[†]These authors contributed equally to this work

1. Experimental procedure

The flow rate of the microfluidic device was governed by the differential hydrostatic pressure between the inlet and the sperm inlet chamber of the device and was regulated by a syringe connected to a holder with adjustable height (Fig. S1). The microscope was encased in a plexiglass box and the temperature inside the box was kept constant at 37 °C using a hot air fan. To ensure the flow rate stability, the fluidic resistance of the device was increased using a meandering channel in the design of the chip. Fig. S2 shows the pressure profile across the

meandering channel at the flow rate of 30 nL/min, simulated using finite element method (FEM). The bulk of the pressure drop occurred in the meandering part of the design and the rest of the device experienced negligible pressure drop. The pressure difference between the inlet and the sperm inlet chamber is 124 Pa as shown in the figure, which translates to approximately 12.7 mm of water column at 37 °C given the expression below,

$$P = \rho g h \tag{S1}$$

where P is liquid pressure, ρ is water density at 37 °C, g is gravity, and h is the height of water column. This height is sufficient to prevent any fluctuations in the fluid flow arising from evaporation or vibration during the experiment.

Fig. S1 The experimental setup included the microscope, the microfluidic device, and the syringe containing mHTF buffered medium. The height of the syringe is adjusted with respect to the device surface to control the flow rate.

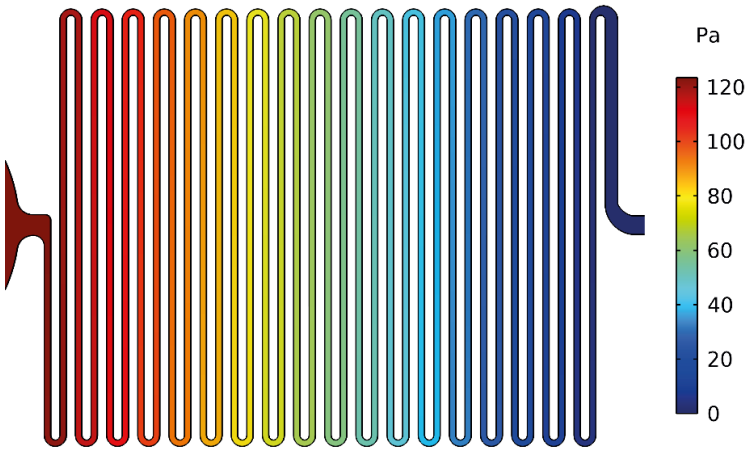

Fig. S2 The pressure difference across the meandering channel. The meandering channel acts as a fluidic resistance, increasing the pressure difference between the inlet and the sperm inlet chamber.

The syringe used in the experiment was a standard 1 mL insulin syringe. For each separate experiment, the medium top surface in the syringe was carefully aligned with the surface of the chip using a laser alignment system. Given the inner diameter of the syringe (4.7 mm) and the desired height difference of 12.7 mm, 220 µL of medium was added to the syringe to make up for the desired height. By doing so, we ensured that the desired pressure difference and thus the flow rate was achieved for the experiment. To validate the accuracy of the aforementioned procedure, micro-particle image velocimetry (µPIV) was conducted using egg yolk diluted in DI water with a concentration of 1%.[1,2] The aforementioned procedure was used for generating the flow rate of 30 nL/min. Fig. S3 shows the results of µPIV analysis compared with FEM simulation.

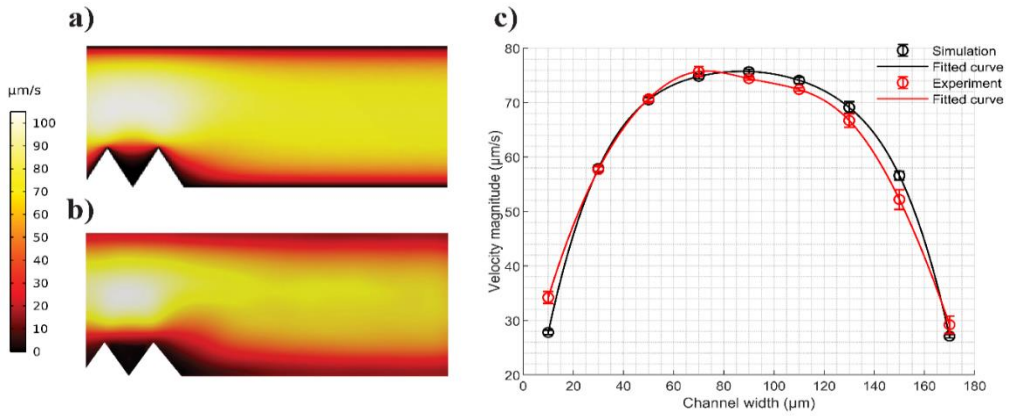

Fig. S3 The velocity field magnitude across the channel at a plane near the middle of channel resulting from (a) FEM numerical analysis (b) experimental (μPIV) analysis. (c) The velocity magnitude across the width of the channel at a plane near the middle of channel for both numerical and experimental analysis (n = 3). The plot clearly illustrates high degree of similarity and relevance between numerical and experimental data and is also validated by a coefficient of determination of R^2 = 0.982, demonstrating a high degree of correlation and reliability between the two analyses.

To further ensure that flow rate stability was maintained during the experiment, evaporation rate of the medium inside the syringe, as one of the main sources of disturbance, was calculated. The evaporation rate is calculated as follows:[3,4]

$$g_h = \theta A(x_s - x) \tag{S2}$$

$$\theta = (25 + 19v) \tag{S3}$$

$$x = 0.62198\frac{p_w}{p_a - p_w} \tag{S4}$$

where g_h is the evaporation rate per hour (kg/h), θ is the evaporation coefficient, A is the exposed water surface area, x_s is the maximum humidity ratio of saturated

air, x is the humidity ratio, v is the air velocity above the water surface, p_w is the partial pressure of the water vapor, and p_a is the atmospheric pressure of the air. Note that given the pure empirical nature of the equations, units of θ do no match. The maximum humidity ratio is achieved when $p_w = p_{ws}$, where p_{ws} is the saturation pressure of water vapor. The value of p_{ws} is related to temperature by the following equation:

$$p_{ws} = \frac{e^{\left(77.345 + 0.0057T - \frac{7235}{T}\right)}}{T^{8.2}} \quad \text{(S5)}$$

where T is the dry bulb temperature of the moist air in Kelvin unit.[3,4]

With a typical relative humidity of 40%, an altitude of 1000 m for the location where experiments were conducted, and an overlaying air velocity of 0.1 m/s, the value of x was found to be 17.9 g/kg using the Mollier diagram.[5] Plugging all the parameters into the equations, the evaporation rate was calculated as 1.07 E-5 kg/h at 37 °C. As the experiments were concluded within 30 minutes, the total amount of evaporated medium equals 5.35 mg, which translates to 5.35 µL. Augmenting this volume with the volume that is lost via the flow into the device (30 nL/min), the total amount of medium that is lost during the experiment equals nearly 6.3 µL. By using the cross-sectional area of the insulin syringe, less than 0.4 mm height of the medium column is reduced, translating to a 3% reduction in flow rate after 30 minutes. This guarantees that the flow rate is indeed reliable and accurate during

the experiment, without utilizing any other instruments and complicating the procedure.

2. Sperm retrieval procedure

We used a slightly modified version of the device for sperm retrieval for SCD and vitality assays. In the modified design, the output pools were designed slightly larger to accommodate the punch holes for extracting the sample out of the pools. In order to keep the fluid from going to the pools, the pools were sealed using scotch tape during the experiment to maintain the desired quiescent condition in the pools. Before the retrieval, the tape was gently removed and the sample was retrieved for further analysis.

3. Sorting thresholds imposed by the barriers

The histogram of the velocity distribution of sperms trapped in pools 1 and 2 along with the fitted Gaussian distributions are shown in Fig. S4a for the flow rate of 30 nL/min. As can be seen, the fitted distribution of the second pool surpasses the first population for V > Upper threshold, where the Upper threshold is V = 74.4 μm/s. In fact, the probability of observing an individual sperm with a velocity higher than that of the threshold is elevated in the second pool which can be interpreted as the

upper limit set by the first constriction. This decision boundary is alike the Bayesian decision boundary which is the optimal decision rule as it minimizes the conditional expected loss. For the lower sorting limit of the first constriction, a similar approach cannot be taken as the distribution of sperm barred from entering the first pool does not obey the Gaussian distribution. Figure S4b shows the distribution of the discarded and accumulated sperms against the population found in the first pool. Accumulated sperms are those that accumulated near the constriction mouth as illustrated in Fig. 6. A lower sorting threshold of V = 46.5 μm/s can be perceived, as the number of sperms found in the first pool surpassed the number of discarded sperms.

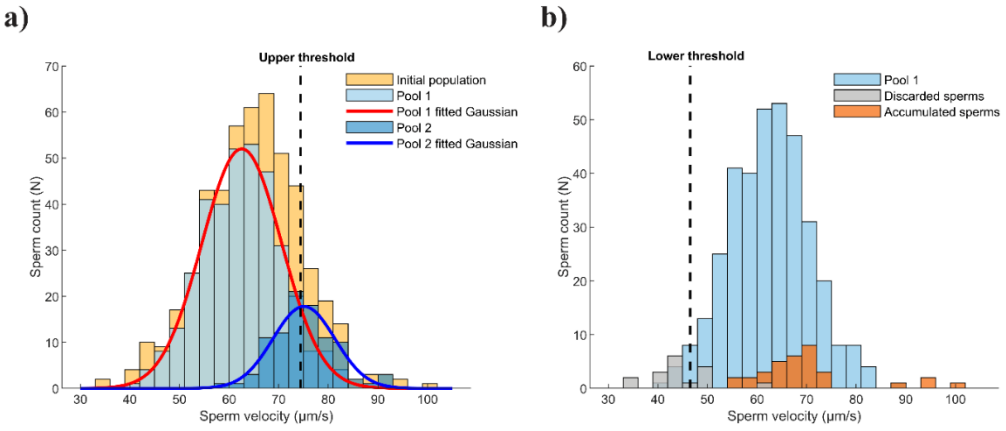

Fig. S4 (a) The histograms of sperms trapped in both pools alongside the two respective fitted Gaussian distributions are shown against the initial population. (b) The histograms of the discarded and accumulated sperms are shown against the population trapped in the first pool. The upper and lower sorting thresholds of the first constriction are illustrated with the dashed line. Sperms with velocities lower or higher than that of the threshold are likely to get discarded or trapped in the second pool, respectively.

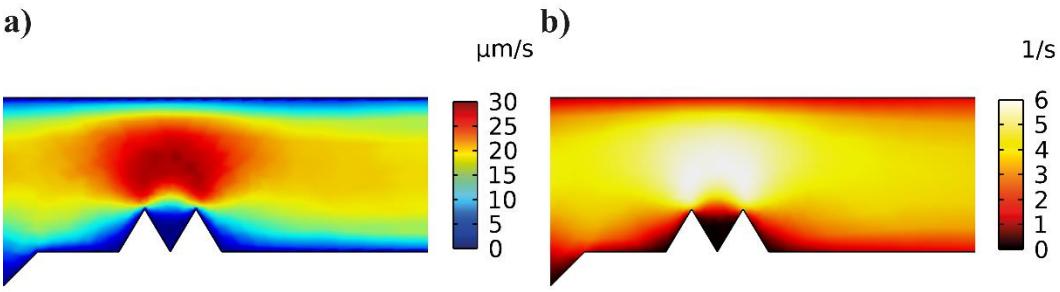

Fig. S5 (a) The velocity field and (b) shear rate profile in the vicinity of the sawtooth-like structure at the flow rate of 30 nL/min. The increase in both the shear rate and the velocity field near the point of the structure creates a favorable condition for sperm detachment.

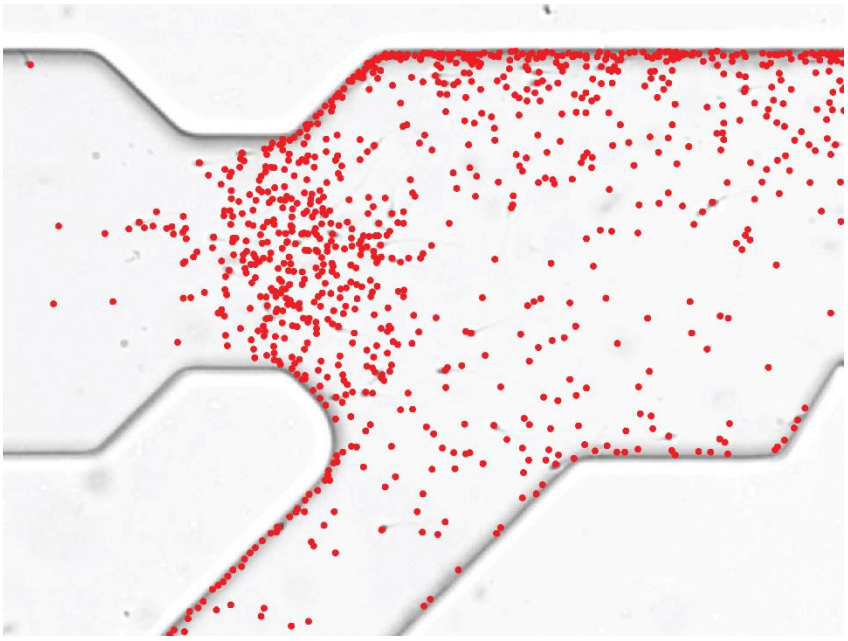

Fig. S6 Dot trajectories of the sperm swimming in the channel in the vicinity of the first constriction. The image illustrates different sperms that follow the upper wall, interact with the structure, pass the structure, and reach the first pool.

Supplementary movies:

Movie S1. Sperm detachment from the sawtooth-like structure. This ensures every sperm faces the hydrodynamic barrier in the device.

Movie S2. Sperm inlet chamber at two different time frames: 1. Immediately following the injection, 2. near the end of the experiment. The movie clearly shows that viable and motile sperms moved out of the chamber, while non-viable, immotile, or extremely low motility sperms along with debris remained in the chamber.

Movie S3. Sperm boundary following behavior through the parallel channels. Viable and motile sperms are guided through these channels to the main sorting channel.

Movie S4. Sperms interactions with the hydrodynamic barrier. Three different interactions are shown in the movie. I. Sperms capable of passing through the barrier. II. Sperms that accumulate near the barrier. III. Sperms that enter the output pool.

Movie S5. Retention of sperms inside the output pool. The movie depicts the most probable area where sperm swims near the pool entrance. The geometry of the pool prevents sperms from swimming out of the pool.

References

1 M. Yaghoobi, M. Azizi, A. Mokhtare, F. Javi and A. Abbaspourrad, *Lab Chip*, 2022, **22**, 1486–1497.

2 K. Pekkan, B. Chang, F. Uslu, K. Mani, C.-Y. Chen and R. Holzman, *Exp. Fluids*, 2016, **57**, 112.

3 L. Shi, Y. Wang, L. Zhang and P. Wang, *J. Mater. Chem. A*, 2017, **5**, 16212–16219.

4 Evaporation from a Water Surface, Engineering Toolbox, https://www.engineeringtoolbox.com/evaporation-water-surface-d_690.html, (accessed 20 December 2023).

5 Mollier diagram, https://www.mollier-diagram.com/, (accessed 20 December 2023).